

# CALPHAD-Guided Prediction and Interpretation of Phase Formation in Ta–Mo–Cr–Ti–Al Refractory High-Entropy Alloys

Kateryna Khanchych,\* Chongchong Tang, Carsten Schroer, Björn Schäfer, Judith Jung, Michael Dürrschnabel, Ute Jäntsche, and Bronislava Gorr

This article presents new results on designing alloys with a disordered body-centered-cubic (BCC) A2 crystal structure within the refractory high-entropy alloy (RHEA) system Ta–Mo–Cr–Ti–Al using equilibrium calculations, microstructure analysis, and differential scanning calorimetry (DSC). Thermodynamic calculation utilizing the calculation of the phase diagrams (CALPHAD) method is applied to predict alloy compositions with a dominant disordered A2 phase, which is considered favorable for enhancing room-temperature ductility. Additionally, the reduced density and improved oxidation resistance are the target properties in the presented alloy design. DSC is used for the identification of the phase transitions taking place upon heating from the room temperature up to 1300 °C. Such phenomena as ordering, phase separation, and higher-order phase transition occurring in two-phase BCC RHEAs are discussed based on the results of microstructural characterization, X-ray diffraction, thermal analysis, and selected area electron diffraction by transmission electron microscopy.

## 1. Introduction

High-entropy alloys (HEA) with a significant proportion of refractory metals refractory high-entropy alloys (RHEAs) have a great potential for high-temperature applications primarily due to their high melting points and mechanical strength at elevated temperatures.<sup>[1]</sup> In body-centered-cubic (BCC) constitution, their yield strength and fracture toughness above 800 °C are competitive with and outperform the nickel-based superalloys currently employed in aviation and aerospace.<sup>[2–4]</sup> The major challenge of RHEAs lies

in their poor low-temperature ductility, high density, and low oxidation resistance.

A major bottleneck in RHEAs development is the scarcity of experimental and theoretical data, which results in an insufficiently accurate thermodynamic assessment of their equilibrium state. The development and continuous refinement of thermodynamic databases are driving progress in designing RHEAs for functional and structural applications.<sup>[5–9]</sup>

Amongst the recently studied RHEA systems is Ta–Mo–Cr–Ti–Al. In complex rutile-type oxide (Cr, Ta, Ti)O<sub>2</sub>, having been identified as a protective oxide for corresponding alloys, Cr and Ta especially contribute to oxidation resistance,<sup>[10]</sup> whereas Ti and Al are beneficial with view on the density of the alloys. The main drawback of Al addition, however, is its tendency to


form various intermetallic phases or induce crystallographic ordering (e.g., B2 phase, CsCl-type), both compromising mechanical performance, especially at low temperature.<sup>[11,12]</sup> Maintaining a disordered BCC crystal structure (A2 phase, W-type) can be considered key for low-temperature ductility,<sup>[13]</sup> though optimum strength is promised by B2 precipitates in a ductile A2 matrix, in analogy to the  $\gamma - \gamma'$  microstructure of the Ni-based superalloys.<sup>[7,14,15]</sup> For instance, 82(TaMoTi)–8Cr–10Al (at%) shows such a structure after annealing at 800, 900 or 1000 °C.<sup>[9]</sup>

The presented study focuses on designing alloys within the Ta–Mo–Cr–Ti–Al system to favor a dominant disordered A2 crystal structure, assuring room-temperature ductility, while targeting a density comparable to conventional nickel-based materials ( $\approx 8 \text{ g cm}^{-3}$ ). Oxidation resistance is likely to be retained. Alloy design is guided by equilibrium phase calculations using the CALPHAD method. Predicted phase constitution and transition temperatures are checked against the results from metallography, including scanning electron microscope (SEM), transmission electron microscopy (TEM), and differential scanning calorimetry (DSC), respectively.

## 2. Experimental Section

In the present work, a commercial software, FactSage 8.2, utilizing the CALPHAD method<sup>[16]</sup> in conjunction with an in-house thermodynamic database, was used for equilibrium state

K. Khanchych, C. Tang, C. Schroer, B. Schäfer, J. Jung, M. Dürrschnabel, U. Jäntsche, B. Gorr  
 Karlsruhe Institute of Technology  
 Institute for Applied Materials – Applied Materials Physics (IAM-AWP)  
 Kaiserstraße 12, 76131 Karlsruhe, Germany  
 E-mail: kateryna.khanchych@kit.edu

 The ORCID identification number(s) for the author(s) of this article can be found under <https://doi.org/10.1002/adem.202500527>.

© 2025 The Author(s). Advanced Engineering Materials published by Wiley-VCH GmbH. This is an open access article under the terms of the Creative Commons Attribution License, which permits use, distribution and reproduction in any medium, provided the original work is properly cited.

DOI: 10.1002/adem.202500527

calculations. The database for the Ta–Mo–Cr–Ti–Al system was developed and experimentally validated by Müller et al.<sup>[17]</sup>

The theoretical density of the identified alloys was calculated according to the rule of mixtures.

$$\rho_{\text{theor}} = \frac{\sum c_i A_i}{\sum \frac{c_i A_i}{\rho_i}} \quad (1)$$

where  $c_i$ ,  $A_i$ , and  $\rho_i$  are the concentration, atomic weight, and density of the element  $i$ .

For the BCC RHEA alloys W–Nb–Mo–Ta and W–Nb–Mo–Ta–V a good agreement has been reported between densities calculated by Equation (1) and those measured for homogenized alloys.<sup>[1]</sup>

A series of Ta–Mo–Cr–Ti–Al alloys, with compositions predefined by the calculations, was manufactured via arc melting using Arc Melter AM/0.5. The produced specimens were button shaped, each with a mass of about 60 g and dimensions of 10 mm in height and  $\approx 40$  mm in diameter. Each button was flipped and remelted at least five times to ensure its homogeneity. High-purity zirconium was used as a getter for residual oxygen, nitrogen, and hydrogen. The chemical compositions of the as-homogenized alloys, as well as levels of interstitial impurities, were determined using the inductively coupled plasma atomic emission spectroscopy (ICP–AES) method. To compensate for the loss of Cr and Al due to evaporation during melting, an excess of 0.2–0.5 g of Cr and up to 0.165 g of Al was added to the respective nominal mixtures. Heat treatment (homogenization) of each specimen was performed in a high-purity Ar flow at 1500 °C for 20 h (parameters previously established).<sup>[11]</sup>

Detailed characteristics of the raw materials used for alloy manufacturing are given in **Table 1**.

The density of the manufactured Ta–Mo–Cr–Ti–Al alloys was measured by Archimedes method using an analytical balance, Mettler Toledo, at 14 °C, offering a measurement accuracy of 0.1 mg. Each sample was measured three times.

Microstructural examination was performed using a high-resolution field-emission scanning electron microscope Zeiss Merlin. Additionally, the microstructural investigation was carried out using a Thermo Fisher Talos F200X TEM equipped with four energy-dispersive X-ray (EDX) detectors and a Gatan Enfium TM electron energy loss spectrometer having 0.8 eV energy resolution. The resolution of the EDX detector was specified by a supplier as  $\leq 136$  eV at Mn-K $\alpha$ . The TEM images and selected area diffraction pattern (SAED) were acquired using a Thermo Fisher Ceta 16 M charge-coupled device (CCD) camera.

**Table 1.** Characteristics of the metals used for alloy manufacturing.

Element	Shape	Purity, [wt%]	Supplier
Ta	pellets	99.9	Evochem
Mo	pellets	99.98	Chempur
Cr	granules	99.94	Chempur
Ti	pellets	99.7	Evochem
Al	granules	99.99	Evochem

Phase constitution was investigated by a Seifert PAD II X-ray diffractometer. X-ray diffraction (XRD) measurements were conducted in a classical Bragg–Brentano geometry ( $\Theta$ – $2\Theta$ ) with a step size of 0.01° and a scan speed of 1°/min was utilized using Cu K $\alpha_1$  radiation ( $\lambda = 0.15406$  nm). The XRD diffractograms were recorded in the  $2\Theta$  range of 20°–100°.

Heat-flux DSC (HF) experiments were conducted using a DSC 404 C Pegasus equipped with a platinum furnace (Netzsch–Gerätebau GmbH (Germany)). Pt–Rh crucibles with lids and Al<sub>2</sub>O<sub>3</sub> inlays were used for the DSC measurements. Two sapphire standards of different masses were employed as reference material for determining the specific isobaric heat capacity  $C_p$  (the derivative of the enthalpy with respect to temperature  $\frac{dH}{dT}$ ). To ensure a high-purity Ar atmosphere, the chamber underwent three cycles of air evacuation prior to introducing Ar gas and establishing a controlled flow, and a Zr getter was mounted on the sample holder to absorb residual oxygen. A baseline was carefully recorded using two empty Pt–Rh crucibles (for the reference material and the sample) at the same Ar flow and heating rate before each series of measurements. A heating–cooling cycle was repeated three times for each specimen to ensure reproducibility and precision of heat flow. All experiments were performed at atmospheric pressure with a heating rate of 10 K min<sup>−1</sup> in the temperature range from the room temperature (RT) up to 1300 °C.

## 3. Results

### 3.1. Equilibrium Calculations

In this section, results of the equilibrium calculations aiming to identify alloys with a dominant disordered A2 crystal structure, reduced density, and favorable oxidation performance within the Ta–Mo–Cr–Ti–Al system are presented.

The equimolar TaMoCrTiAl alloy serves as the starting point in searching for compositions with tailored properties. It is well established that at RT, after homogenization at 1400 °C for 20 h, this alloy consists of an ordered B2 matrix with precipitates of the intermetallic Laves phase Cr<sub>2</sub>Ta (C15) (area proportion of the Laves phase is  $\approx 20\%$ ).<sup>[17]</sup> At  $\approx 1060$  °C, an A2-to-B2 higher-order phase transition takes place, and a disordered A2 becomes the only stable phase (Figure S1, Supporting Information). The authors<sup>[17]</sup> claim that the stabilization of the B2 phase at lower temperatures is due to the increased Al content. To effectively decrease the A2-to-B2 transformation temperature, it was suggested to keep Al concentration below 15 at%.<sup>[17]</sup> To suppress the Laves phase formation, it is natural to reduce the Cr and/or Ta concentrations.

In order to identify alloy compositions with a dominant disordered A2 phase in combination with reduced density and adequate oxidation resistance, the following optimization criteria are selected. 1) **Phase Stability:** The molar fraction of the disordered A2 phase ( $x_{A2}$ ) in the temperature range of 700–1000 °C should be  $x_{A2} \geq 0.94$  (i.e., nearly single-phase). 2) **Composition Balance:** To fulfill Criterion 1, Cr and Al atomic concentrations should be decreased in order to suppress the formation of the Laves phase and the ordered B2, respectively. At the same time, to maintain adequate oxidation resistance,

Cr and Al content should be kept reasonably high. 3) **Density Reduction:** To decrease the density of the alloy satisfies the two aforementioned criteria, Ta concentration should be minimized by increasing Mo (step 1) and Ti (step 2).

Criterion 1 is established with the understanding that completely avoiding the formation of the Laves phase at intermediate temperatures is not feasible even at minimal Cr concentration (5 at%) according to equilibrium calculations. A possible way to suppress the formation of the Laves phase is to apply a sufficiently high homogenization temperature.<sup>[11]</sup>

The upper limit of 1000 °C in Criterion 1 is guided by the theoretical A2-to-B2 transformation temperature for the equimolar TaMoCrTiAl alloy and the experimentally proven stability of the B2 phase up to 1000 °C.<sup>[9]</sup> The lower temperature limit (700 °C) is set under the assumption of a negligible diffusion below 700 °C, which would prevent the formation of brittle phases if their equilibrium phase fractions are relatively low.

At first, the effect of Al and Cr on the phase equilibrium is estimated separately. The minimal concentrations of both elements were set to 5 at% due to the need to maintain adequate oxidation resistance and varied up to 20 at%. For the alloy series (95-x)(TaMoTi)-5Cr-xAl (Figure 1a), the calculation predicts a phase diagram consisting of four regions a three-phase field (A2 + B2 + C15) at lower temperatures, two-phase fields (A2 + C15/B2 + C15) up to ≈1100 °C depending on Al concentration, and single-phase A2 above 1100 °C at Cr concentration up to 20 at%.

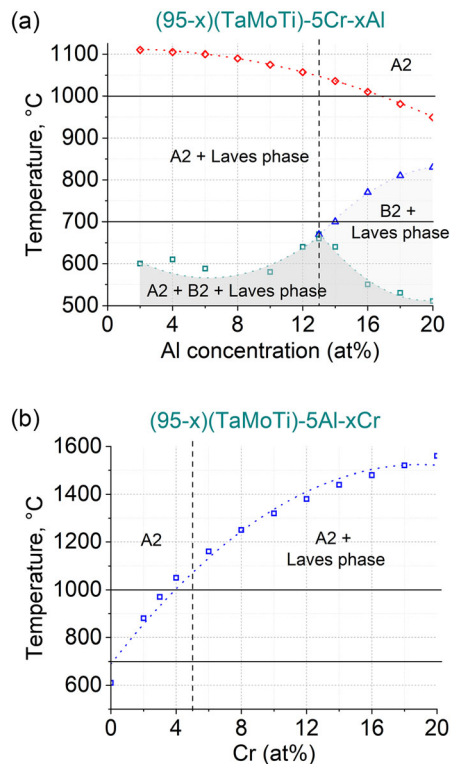


**Figure 1.** The effects of a) Al and b) Cr concentrations on the equilibrium phase composition in Ta-Mo-Cr-Ti-Al alloys (only data below liquidus temperatures are shown).

A phase diagram of the alloy series (95-x)(TaMoTi)-5Al-xCr (Figure 1b) consists of two areas—a single-phase A2 and a two-phase A2 + C15. According to the equilibrium calculations, the

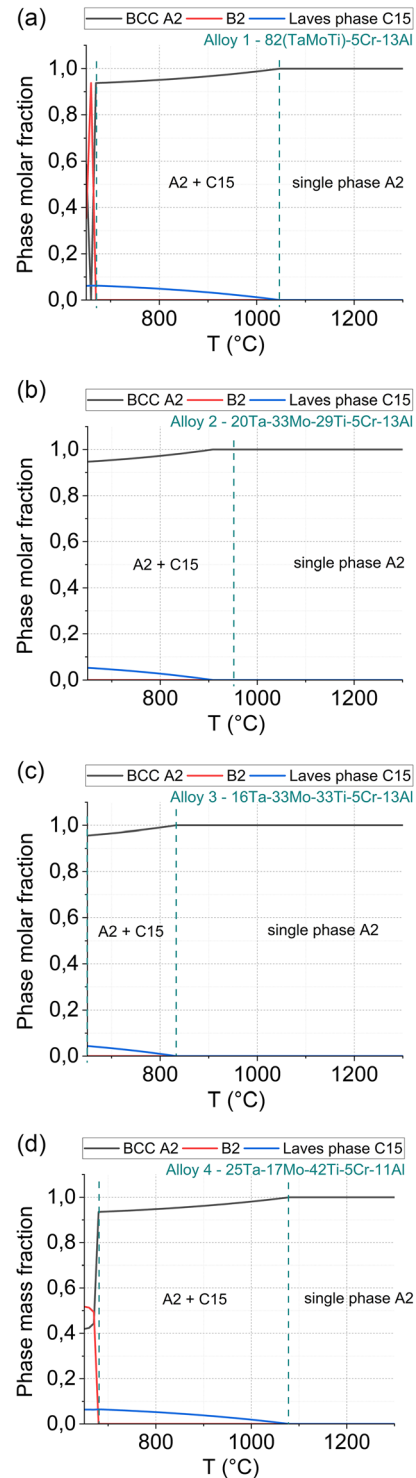


**Figure 2.** Predicted equilibrium phase compositions of a) 82(TaMoTi)-5Cr-13Al (Alloy 1); b) 20Ta-33Mo-29Ti-5Cr-13Al (Alloy 2); c) 16Ta-33Mo-33Ti-5Cr-13Al (Alloy 3); and d) 25Ta-17Mo-42Ti-5Cr-11Al (Alloy 4). Dashed lines indicate the phase transitions.

content of the Laves phase grows steeply with increasing Cr concentration. Only data below the liquidus temperatures are shown. The liquidus temperatures of the identified alloys lie in the range of 2190–2280 °C.

The calculation results reveal that to satisfy Criteria 1 and 2, the Al concentration should not exceed 13 at% (which is in agreement with the previously reported limitation 15 at%),<sup>[17]</sup> and the Cr concentration should be limited to 5 at%.

Following up on Criteria 1–3, four promising alloy compositions were identified.

$$\begin{aligned} 82(\text{TaMoTi})\text{--}5\text{Cr}\text{--}13\text{Al (Alloy 1)} & \left( \rho_{\text{theor}} = 9.25 \frac{\text{g}}{\text{cm}^3} \right) \\ 20\text{Ta}\text{--}33\text{Mo}\text{--}29\text{Ti}\text{--}5\text{Cr}\text{--}13\text{Al (Alloy 2)} & \left( \rho_{\text{theor}} = 8.68 \frac{\text{g}}{\text{cm}^3} \right) \\ 16\text{Ta}\text{--}33\text{Mo}\text{--}33\text{Ti}\text{--}5\text{Cr}\text{--}13\text{Al (Alloy 3)} & \left( \rho_{\text{theor}} = 8.16 \frac{\text{g}}{\text{cm}^3} \right) \\ 25\text{Ta}\text{--}17\text{Mo}\text{--}42\text{Ti}\text{--}5\text{Cr}\text{--}11\text{Al (Alloy 4)} & \left( \rho_{\text{theor}} = 8.50 \frac{\text{g}}{\text{cm}^3} \right) \end{aligned}$$

The composition of Alloy 1 is derived directly from **Figure 1a** and **2a**, which restrict the content of the A2 phase in accordance with Criteria 1 and 2. It should be noted that the concentration of aluminum was selected at its upper allowable limit to reduce density and increase oxidation resistance.

The composition of Alloy 2 follows from a combination of Criteria 1–2 and addresses Criterion 3 (step 1), wherein a decrease in Ta content is primarily compensated by increasing Mo.

In a similar way, the concentration of the Alloy 3 follows from a combination of Criteria 1–2 and Criterion 3 (step 2), suggesting a further decrease in Ta content offset by increased Ti fraction.

The composition of the Alloy 4 follows from Criteria 1–2 and available literature data on the experimentally confirmed plasticity of the ternary alloy 30Ta–20Mo–50Ti (at%),<sup>[18]</sup> from which the Ta:Mo:Ti ratio was derived. The Alloy 4 has a reduced Al concentration (11 at%) compared to the other three alloys (containing 13 at% Al).

The calculated equilibrium molar fractions of the phases in the newly identified Ta–Mo–Ti–Cr–Al alloys are presented in **Figure 2**.

It should be mentioned that the equilibrium calculation for all the candidate Ta–Mo–Cr–Ti–Al alloys predicts the formation of the stable B2 phase at lower temperatures: below 670 °C for Alloy 1, below 620 °C for Alloy 2 (out of the range shown in **Figure 2b**), below 650 °C for Alloy 3 (out of the range shown in **Figure 2c**), and below 680 °C for Alloy 4. Therefore, the kinetics of the B2 formation, as well as the possibility to retain the high-temperature A2 crystal structure until RT, need to be studied.

## 3.2. Chemical Composition and Microstructure

### 3.2.1. Chemical Composition

The nominal chemical composition of the manufactured and homogenized alloys was determined by the ICP–AES method and is presented in **Table 2**. The measured compositions of the produced alloys closely match the targeted nominal values. The registered level of dissolved oxygen is up to  $184 \pm 45$  wppm for Alloys 1–3, but two times higher for Alloy 4 ( $406 \pm 79$  wppm). These values are considered acceptable. The level of nitrogen in the produced alloys is negligibly low, up to  $33 \pm 8$  wppm.

The respective densities of the Ta–Mo–Cr–Ti–Al alloys are presented in **Table 3**.

### 3.2.2. SEM Backscatter (BSE) Imaging

SEM backscatter (BSE) imaging only reveals a single phase (see **Figure 3**). No precipitates of the Laves phase are observed either within the grains or at the grain boundaries. Significant porosity occurring during casting and homogenization can be related to a Kirkendall effect.<sup>[19]</sup> The average grain sizes determined by the surface area are 155  $\mu\text{m}$  (Alloy 1), 85  $\mu\text{m}$  (Alloy 2), 170  $\mu\text{m}$  (Alloy 3), and 285  $\mu\text{m}$  (Alloy 4), respectively.

### 3.2.3. Phase Constitution by X-ray Diffraction

The XRD patterns of the produced alloys in the as-homogenized condition are shown in **Figure 4**. Four major Bragg peaks of the BCC phase are identified in each sample. Minor peaks appearing on all the XRD patterns (insets in **Figure 4**) can be attributed to the B2 phase, however, their intensity is insufficient for its unambiguous detection. Variations in peak intensity are likely due to grain orientation effects. The lattice constants of the investigated

**Table 3.** Calculated and measured density of the Ta–Mo–Cr–Ti–Al alloys.

Nominal chemical composition	Designation	$\rho_{\text{theor}} [\text{g cm}^{-3}]$	$\rho_{\text{exp}} [\text{g cm}^{-3}]$
82(TaMoTi)5 Cr13Al	Alloy 1	9.25	9.35
20Ta33Mo29Ti5Cr13Al	Alloy 2	8.68	8.66
16Ta33Mo33Ti5Cr13Al	Alloy 3	8.16	8.15
25Ta17Mo42Ti5Cr11Al	Alloy 4	8.50	8.62
20Ta20Mo20Cr20Ti20Al	Equimolar TaMoCrTiAl	8.41	8.60

**Table 2.** Nominal and measured chemical compositions (in at%) (ICP–AES) of the manufactured alloys.

Nominal chemical composition	Designation	x [at%]					x [wppm]	
		Ta	Mo	Ti	Cr	Al	O	N
82(TaMoTi)5Cr13Al	Alloy 1	26.16	26.41	26.55	6.72	14.16	$105 \pm 26$	$30 \pm 7$
20Ta33Mo29Ti5Cr13Al	Alloy 2	18.77	32.94	29.45	6.33	12.51	$130 \pm 32$	$32 \pm 8$
16Ta33Mo33Ti5Cr13Al	Alloy 3	15.23	32.09	34.04	6.19	12.44	$184 \pm 45$	$33 \pm 8$
25Ta17Mo42Ti5Cr11Al	Alloy 4	24.34	16.84	42.03	6.16	10.63	$406 \pm 79$	$30 \pm 7$

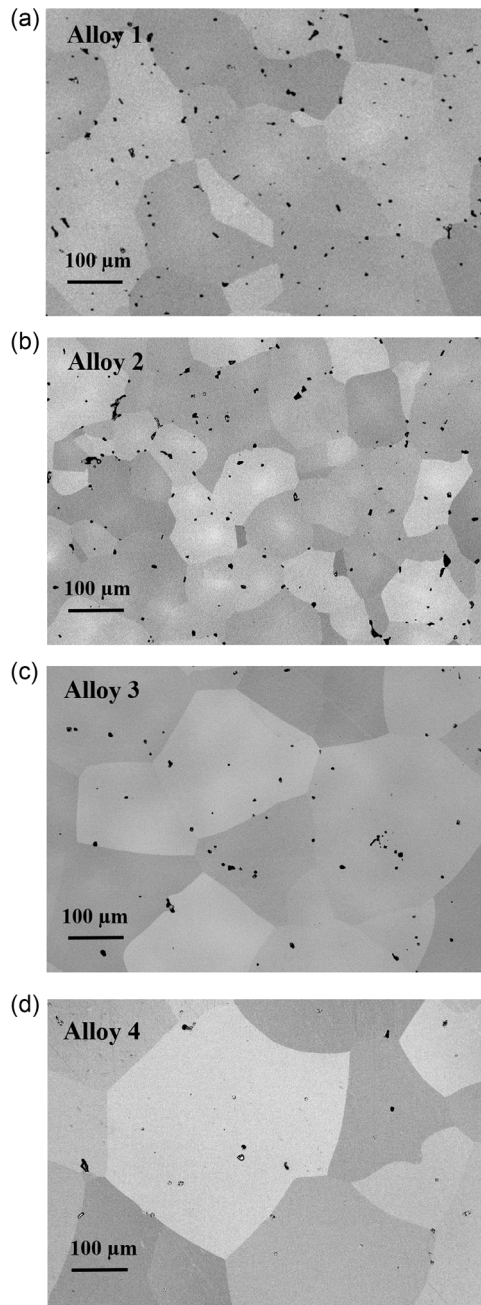


**Figure 3.** BSE micrographs (orientation contrast) of the investigated alloys within the TaMoCrTiAl system in as-homogenized state: a) 82(TaMoTi)–5Cr–13Al (Alloy 1); b) 20Ta–33Mo–29Ti–5Cr–13Al (Alloy 2); c) 16Ta–33Mo–33Ti–5Cr–13Al (Alloy 3); and d) 25Ta–17Mo–42Ti–5Cr–11Al (Alloy 4). Black features are pores that arise during casting and homogenization.

alloys are in the range of 3.175–3.217 Å. Diffraction peaks from the Laves phase C15 are not detected.

### 3.2.4. TEM Analysis

A bright-field TEM image and corresponding SAED pattern of Alloy 4 (25Ta-17Mo-42Ti-5Cr-11Al) are presented in **Figure 5a,b**,

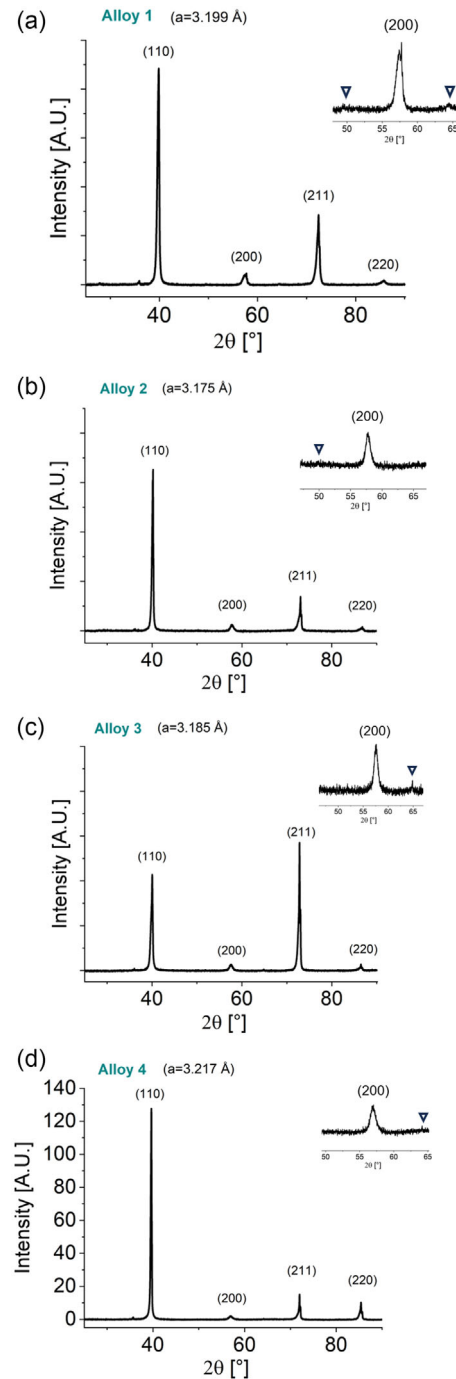


**Figure 4.** XRD diffractograms of the as-homogenized alloys: a) Alloy 1; b) Alloy 2; c) Alloy 3; and d) Alloy 4. A small peak next to (110) is related to a residual  $K_{\beta}$  radiation.

respectively. SAED reveals a two-phase microstructure with strong A2 reflections and weak B2 superlattice reflections (marked with triangles). The SAED intensity line profile (LP) (Figure 5c) shows that the intensity of B2 reflections is at least three orders of magnitude lower than that of A2, confirming A2 as a primary phase. The B2 reflections are also observed in the fast Fourier transform (FFT) (Figure 5e,f) of the high-resolution

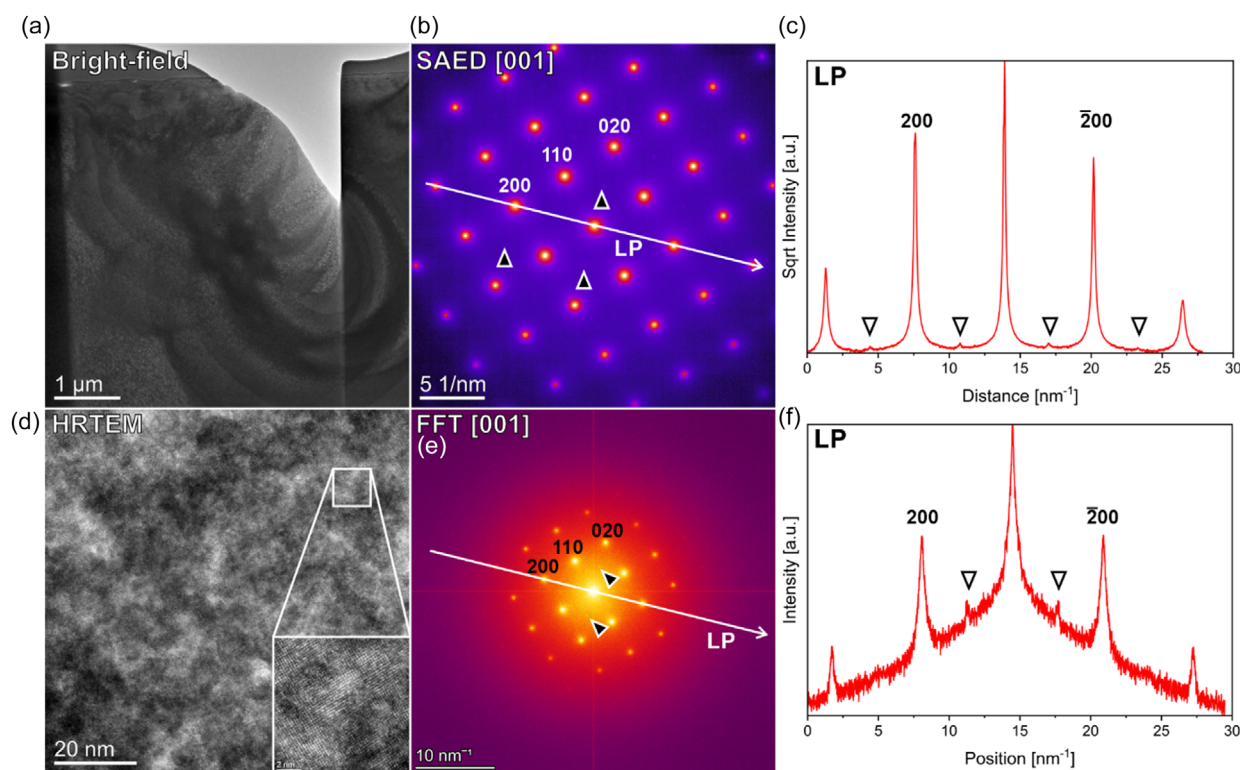


**Figure 5.** a) Bright-field TEM image acquired from Alloy 4 (25Ta–17Mo–42Ti–5Cr–11Al); b) corresponding SAED pattern from the  $[001]_{\text{BCC}}$  zone axis, displayed in false colors; c) SAED intensity LP; d) TEM high-resolution phase contrast image (HRTEM), e) corresponding FFT analysis, as well as f) FFT intensity LP.

phase contrast TEM image (Figure 5d). It is hypothesized that weak superstructure reflections observed in both SAED and FTT analyses originate from the presence of nanosized B2 domains embedded within the disordered A2 matrix. Such a nanostructured B2-in-A2 phase arrangement has been previously reported in multicomponent alloys exhibiting local chemical ordering and may resemble the  $\gamma - \gamma'$  microstructure known in Ni-based superalloys.<sup>[14]</sup> The only reported study of the formation and thermal stability of a two-phase A2–B2 microstructure in the alloys within the Ta–Mo–Cr–Ti–Al system is available for 82(TaMoTi)–8Cr–10Al (at%) alloy composition,<sup>[9]</sup> which does not provide sufficient evidence to support our hypothesis based on existing literature. Senkov et al. reported a microstructure comprising a disordered BCC A2 matrix with ordered B2 nanoprecipitates for another RHEA with the composition AlMo0.5NbTa0.5TiZr.<sup>[20]</sup> It should be mentioned that the surface damage by focused ion beam preparation may to some extent, obstruct the nanodomain contrast, which hinders the possibility of spatial separation of the two phases on the atomic resolution level.

Scanning transmission electron microscopy–high-angle-annular dark-field (STEM–HAADF) imaging and corresponding EDX elemental mapping of Alloy 4 (Figure 6a) were used to identify local compositional variations. STEM/EDX reveals slight local variations in Ti, Ta, and Al concentration (Figure 6a). The EDX LP (Figure 6b) reveals 14 nm-sized areas enriched in Ti and Al and depleted in Ta, with corresponding depletion (Ti, Al) and enrichment (Ta) at the fringes. Mo and Cr are rather homogeneously distributed within the analyzed region.

If assuming that the nanoscale B2 domains are chemically distinct, enriched in Ti and Al, and depleted in Ta, the observed compositional variations align well with the predicted B2 phase composition from equilibrium calculations (Figure 7).

### 3.3. Thermal Analysis

After confirming the microstructure and phase composition of the Alloys 1–4 in the as-homogenized state, HF-DSC was utilized to investigate phase transformations upon heating in the temperature range from 200 to 1300 °C. The obtained  $\frac{dH}{dT}$  curves are presented in Figure 8. Distinct endothermic peaks are observed in all DSC curves: for Alloys 1 and 3, the curves show two overlapping peaks, and only a single peak in the case of Alloys 2 and 4. Extended plateau regions with increased  $\frac{dH}{dT}$  preceding the first peak are observed for Alloy 1 and 3.

As mentioned before, in the Ta–Mo–Cr–Ti–Al system, such phenomena as ordering, phase separation, and higher-order phase transition can occur.<sup>[11,12]</sup> The formation and successive degradation of the Laves phase predicted by equilibrium calculations while heating cannot be excluded as well.

Schematic binary phase diagram between the pure disordered A2 and ordered B2 phases for complex concentrated alloys and HEA was first reported by Naka and Khan<sup>[21]</sup> and later updated by Lass.<sup>[22]</sup> In both papers, it is established that below the liquidus temperature A2–B2 phase diagram consists of three areas: single-phase disordered A2 and pure single-phase ordered B2 phase separated by a higher-order transition line and a two-phase region

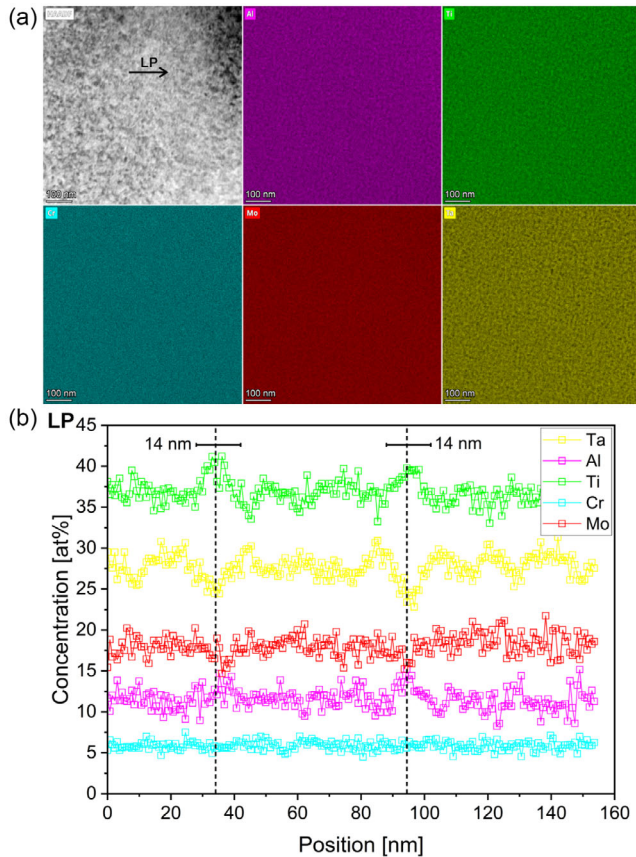


**Figure 6.** a) STEM image with respective EDX element mapping and b) concentration line profiles of Alloy 4 (25Ta–17Mo–42Ti–5Cr–11Al).

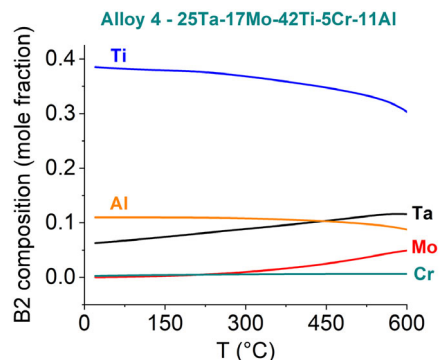


**Figure 7.** Calculated equilibrium composition of the B2 phase in Alloy 4 as a function of temperature between RT and 600 °C.

A2 + B2 at lower temperatures. Lass<sup>[22]</sup> additionally suggested that the two-phase region A2 + B2 may consist of three subregions depending on the phase separation type: the region of spinodal-like decomposition and two neighboring regions, where the phase separation occurs according to the nucleation and growth mechanism (see Figure S2, Supporting Information). Since distinguishing between these three possible subregions of A2–B2 phase field for the Ta–Mo–Cr–Ti–Al system is currently experimentally unresolved, the available database used in the current article is based on

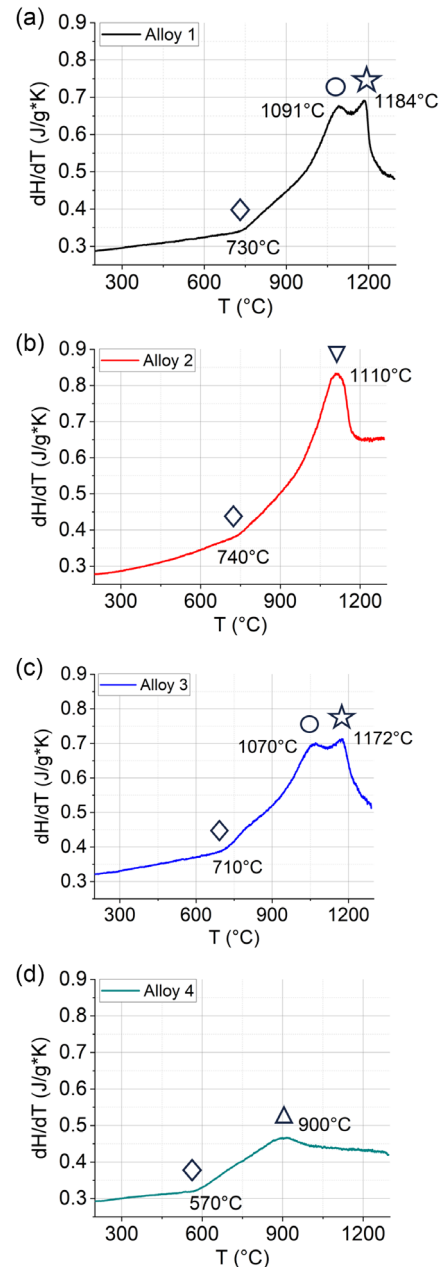


**Figure 8.** Temperature derivative of the enthalpy  $\frac{dH}{dT}$  of the Alloys 1–4 in as-homogenized state: a) 82(TaMoTi)–5Cr–13Al (Alloy 1); b) 20Ta–33Mo–29Ti–5Cr–13Al (Alloy 2); c) 16Ta–33Mo–33Ti–5Cr–13Al (Alloy 3); and d) 25Ta–17Mo–42Ti–5Cr–11Al (Alloy 4). Markers denote the onsets and reactions occurring in the alloys:  $\diamond$ —the onset;  $\circ$  and  $\star$  mark the first and the second consequent reactions taking place in Alloys 1 and 3;  $\nabla$  and  $\triangle$  mark the reactions taking place in Alloy 2 and 4, respectively.

the phase diagram type suggested in another study.<sup>[21]</sup> Thus, the performed thermal analysis aims to detect transition temperatures between the A2–B2 field and single-phase A2 and B2 fields in the studied Ta–Mo–Cr–Ti–Al alloys.

It should be noted that since all DSC data were obtained at the same heating/cooling rate, the influence of diffusion on phase

transformations has not been studied, which may result in discrepancies between the transition temperatures obtained experimentally and calculated for the equilibrium state. Additionally, the equilibrium conditions of the alloys in the studied temperature range need to be further verified with reference to the calculations performed.

The DSC curves of the equimolar TaMoTiCrAl alloy, both reported by Chen et al.<sup>[11]</sup> and measured in the present work (Figure S3, Supporting Information), contain one peak having a so-called  $\lambda$ -shape at the temperature 1106 °C (1109 °C in.<sup>[11]</sup> According to the calculation (Figure S1, Supporting Information), a higher-order A2–B2 phase transition is expected in this temperature range, B2  $\rightarrow$  A2. However, the experimentally observed phase transition temperature is 56 °C higher than the calculated one. Thus, according to the shape<sup>[23]</sup> and position, this DSC peak can be assigned to the expected A2–B2 higher-order phase transition.

The DSC curves of Alloys 1 and 3 (Figure 8a,c) contain two overlapping peaks (1091 °C and 1184 °C for Alloy 1, 1070 °C and 1172 °C for Alloy 3, respectively), indicating a complex phase transition. On the respective calculated plots (Figure 2a,c), the only one phase transition predicted in this temperature range is A2 + C15  $\rightarrow$  A2, while A2 + B2  $\rightarrow$  A2 transition is expected at much lower temperatures. The predicted temperatures of A2 + B2  $\rightarrow$  A2 transition are 670 °C for Alloy 1 and 650 °C for Alloy 3, respectively; the predicted temperatures of A2 + C15  $\rightarrow$  A2 phase transitions are 1060 °C for Alloy 1 and 840 °C for Alloy 3, respectively. Obviously, the observed DSC peaks cannot be rationalized based on the results of equilibrium calculations.

The DSC curves of Alloys 2 and 4 (Figure 8b,d) reveal one endothermic peak each, at around 1110 °C for Alloy 2 and 900 °C for Alloy 4, which indicates one phase transition. In the case of Alloy 4, the peak is significantly less pronounced and appears at a lower temperature. The respective calculated temperatures of the phase transitions expected in this temperature range (Figure 2b,d) are 910 °C for Alloy 2 and 1080 °C for Alloy 4, which is not in line with the observations. The peaks appearing on the DCS heating curves of Alloys 2 and 4 are likely related to the ordering phase transition A2 + B2  $\rightarrow$  A2, which, however, follows different pathways depending on the initial degree of the ordering. As in the case of Alloys 1 and 3, the observed features of the DCS heating curves for Alloys 2 and 4 cannot be rationally explained in the current state of research.

Based on the most recent phase diagram for A2–B2 compositionally complex alloys reported by Lass<sup>[22]</sup> (Figure S2, Supporting Information), the phase transitions observed in DSC curves for Alloys 1 and 3 could occur due to the following path: upon heating, both alloys initially in the A2 + B2 field (covering  $\alpha_2$  and  $\beta_2$  subregions) undergo two transitions: first to a B2-dominant  $\beta_1$  phase, then to a single-phase A2 structure. The second,  $\lambda$ -shaped peak suggests a higher-order  $\beta_1 \rightarrow$  A2 transition, also seen in equimolar TaMoTiCrAl. For Alloys 2 and 4, heating likely causes a transition from  $\alpha_1$  or the  $\beta_2$  region of the A2 + B2 field to A2.

## 4. Discussion

Microstructural characterization (Figure 3) highlights the limitations of SEM in resolving A2–B2 phase constitution in

Ta–Mo–Cr–Ti–Al alloys. The formation of the Laves phase is apparently inhibited by a high homogenization temperature and fast cooling, which is in agreement with the calculations (Figure 2) and assumed kinetic aspects. The phase stability of the produced alloys needs to be checked by a longer heat treatment.

XRD analysis (Figure 4) confirms that the microstructure of the investigated Ta–Mo–Cr–Ti–Al alloys is predominantly composed of a disordered A2 phase with minor superlattice peaks apparently generated by the ordered B2 phase, which is in agreement with the thermodynamic predictions (Figure 2).

In support of XRD results, TEM analysis utilizing SAED performed on the Alloy 4 (25Ta–17Mo–42Ti–5Cr–11Al) (Figure 5) reveals a two-phase microstructure, providing further support for the coexistence of A2 and B2 phases. Since Alloy 4 was investigated at RT in the as-homogenized state, this result complies with the calculated phase composition predicting the presence of the stable B2 phase along with the A2 phase at <600 °C (Figure 2d). Thus, a necessity of the use of high-resolution TEM and atom probe tomography for the accurate experimental investigation of the microstructure of two-phase Ta–Mo–Cr–Ti–Al alloys can be stated.

The results of the thermal analysis performed by HF-DSC (Figure 8) reveal a complex phase transition behavior in the investigated Ta–Mo–Cr–Ti–Al alloys. The observed thermal events are presumably related to a disorder transition as well as a higher-order A2–B2 phase transformation. The phenomenon of phase separation is not experimentally confirmed and needs to be further investigated. The discrepancy between the observed phase transition temperatures and those predicted by equilibrium calculation may stem from the limitations in the current thermodynamic assessment of the Ta–Mo–Cr–Ti–Al system, particularly regarding the A2–B2 two-phase phase region and from kinetic factors influencing phase evolution. These aspects merit further investigation to enhance the predictive capability for phase stability in this RHEA system.

## 5. Conclusions

Based on the equilibrium calculations combined with microstructural analysis and calorimetric study of the newly developed alloys within the Ta–Mo–Cr–Ti–Al system, the following conclusions can be drawn. 1) The calculation aiming to design alloys with a dominant disordered A2 phase, reduced density, and favorable oxidation performance yields four chemical compositions with respective densities between 8.16 and 9.25 g cm<sup>−3</sup>. 2) According to the equilibrium calculations, to assure the formation of a dominant disordered A2 phase at moderate temperatures, concentrations of Al and Cr must be limited to 13 at% and 5 at%, respectively. This compromises the reduction of the density and improvement of the oxidation resistance of the alloys. The formation of the Laves phase C15 at RT is likely suppressed. 3) TEM analysis confirms a two-phase microstructure of Alloy 4 (25Ta–17Mo–42Ti–5Cr–11Al) at RT, presumably consisting of a disordered A2 phase matrix with embedded nanosized B2 phase domains. 4) DSC curves of Alloys 1 (82(TaMoTi)–5Cr–13Al) and

3 (16Ta–33Mo–33Ti–5Cr–13Al) exhibit two overlapping peaks, likely indicating a complex ordering phase transition involving A2–B2 phase transformation, while Alloys 2 (20Ta–33Mo–29Ti–5Cr–13Al) and 4 (25Ta–17Mo–42Ti–5Cr–11Al) exhibit one peak each, likely related to the ordering phase transition.

Received: February 23, 2025

Revised: April 18, 2025

Published online:

## Supporting Information

Supporting Information is available from the Wiley Online Library or from the author.

## Acknowledgements

This work was funded by the Federal Ministry for Economic Affairs and Climate Action of Germany (now Federal Ministry for Economic Affairs and Energy) (project number 20E2112B) and linked to the Materials and Technologies for the Energy Transition Program of the Helmholtz Association. The authors thank Dr. Thomas Bergfeldt and Tatjana Kaiser for performing chemical analysis.

Open Access funding enabled and organized by Projekt DEAL.

## Conflict of Interest

The authors declare no conflict of interest.

## Author Contributions

**Kateryna Khanchych:** investigation (lead); writing—original draft (lead). **Chongchong Tang:** supervision (supporting); writing—review and editing (supporting). **Carsten Schroer:** supervision (supporting); writing—review and editing (supporting). **Björn Schäfer:** methodology (supporting). **Judith Jung:** data curation (supporting); methodology (supporting). **Michael Dürschnabel:** data curation (supporting); investigation (supporting); **Ute Jäntsche:** methodology (supporting). **Bronislava Gorr:** conceptualization (lead); resources (lead); writing—review and editing (supporting).

## Data Availability Statement

The data that support the findings of this study are available from the corresponding author upon reasonable request.

## Keywords

calculation of the phase diagrams, differential scanning calorimetry, microstructures, Ta–Mo–Cr–Ti–Al, transmission electron microscopy

- [1] O. N. Senkov, G. B. Wilks, D. B. Miracle, C. P. Chuang, P. K. Liaw, *Intermetallics* **2010**, *18*, 1758.
- [2] Y. Zhang, T. T. Zuo, Z. Tang, M. C. Gao, K. A. Dahmen, P. K. Liaw, Z. P. Lu, *Prog. Mater. Sci.* **2014**, *61*, 1.
- [3] O. N. Senkov, S. Gorsse, D. B. Miracle, *Acta Mater.* **2019**, *175*, 394.
- [4] O. N. Senkov, G. B. Wilks, J. M. Scott, D. B. Miracle, *Intermetallics* **2011**, *19*, 698.
- [5] S. Gorsse, D. B. Miracle, O. N. Senkov, *Acta Mater.* **2017**, *135*, 177.
- [6] D. B. Miracle, O. N. Senkov, *Acta Mater.* **2017**, *122*, 448.
- [7] D. B. Miracle, M. H. Tsai, O. N. Senkov, V. Soni, R. Banerjee, *Scr. Mater.* **2020**, *187*, 445.
- [8] O. N. Senkov, D. B. Miracle, K. J. Chaput, J. P. Couzinie, *J. Mater. Res.* **2018**, *33*, 3092.
- [9] S. Laube, A. Kauffmann, S. Schellert, S. Seils, A. S. Tirunilai, C. Greiner, Y. M. Eggeler, B. Gorr, H. J. Christ, M. Heilmaier, *Sci. Technol. Adv. Mater.* **2022**, *23*, 692.
- [10] S. Schellert, M. Weber, H. J. Christ, C. Wiktor, B. Butz, M. C. Galetz, S. Laube, A. Kauffmann, M. Heilmaier, B. Gorr, *Corros. Sci.* **2023**, *211*, 110885.
- [11] H. Chen, A. Kauffmann, S. Seils, T. Boll, C. H. Liebscher, I. Harding, K. S. Kumar, D. V. Szabó, S. Schlabach, S. Kauffmann-Weiss, F. Müller, *Acta Mater.* **2019**, *176*, 123.
- [12] S. Laube, S. Schellert, A. S. Tirunilai, D. Schliephake, B. Gorr, H. J. Christ, A. Kauffmann, M. Heilmaier, *Acta Mater.* **2021**, *218*, 117217.
- [13] S. Laube, H. Chen, A. Kauffmann, S. Schellert, F. Müller, B. Gorr, J. Müller, B. Butz, H. J. Christ, M. Heilmaier, *J. Alloys Compd.* **2020**, *823*, 153805.
- [14] K. Ma, T. Blackburn, J. P. Magnussen, M. Kerbstadt, P. A. Ferreira, T. Pinomaa, C. Hofer, D. G. Hopkinson, S. J. Day, P. A. Bagot, M. P. Moody, *Acta Mater.* **2023**, *257*, 119183.
- [15] A. J. Knowles, D. Dye, R. J. Dodds, A. Watson, C. D. Hardie, S. A. Humphry-Baker, *Appl. Mater. Today* **2021**, *23*, 101014.
- [16] H. Lukas, S. G. Fries, B. Sundman, *Computational Thermodynamics: The Calphad Method*, Cambridge University Press, USA **2007**.
- [17] F. Müller, B. Gorr, H. J. Christ, H. Chen, A. Kauffmann, S. Laube, M. Heilmaier, *J. Alloys Compd.* **2020**, *842*, 155726.
- [18] E. Delvat, D. M. Gordin, T. Gloriant, J. L. Duval, M. D. Nagel, *J. Mech. Behav. Biomed. Mater.* **2008**, *1*, 345.
- [19] R. W. Balluffi, L. L. Seigles, *Acta Metall.* **1957**, *5*, 449.
- [20] O. N. Senkov, J. K. Jensen, A. L. Pilchak, D. B. Miracle, H. L. Fraser, *Mater. Des.* **2018**, *139*, 498.
- [21] S. Naka, T. Khan, *J. Phase Equilib.* **1997**, *18*, 635.
- [22] E. A. Lass, *Metall. Mater. Trans. A Phys. Metall. Mater. Sci.* **2022**, *53*, 4481.
- [23] R. Santamarta, E. Cesari, J. Font, J. Muntasell, J. Pons, J. Dutkiewicz, *Scr. Mater.* **2006**, *54*, 1985.